Semiclassical description of photoionization microscopy

Ch. Bordas and F. Lépine

Laboratoire de Spectrométrie Ionique et Moléculaire, UMR CNRS 5579, Bâtiment A. Kastler, 43 Boulevard du 11 Novembre 1918, 69622 Villeurbanne Cedex, France

C. Nicole* and M. J. J. Vrakking

FOM Instituut voor Atoom en Molecuul Fysica (AMOLF), Kruislaan 407, 1098 SJ Amsterdam, The Netherlands

Recently, experiments have been reported where a geometrical interference pattern was observed when photoelectrons ejected in the threshold photoionization of xenon were detected in a velocity-map imaging apparatus [C. Nicole *et al.*, Phys. Rev. Lett. **88**, 133001 (2002)]. This technique, called photoionization microscopy, relies on the existence of interferences between various trajectories by which the electron moves from the atom to the plane of observation. Unlike previous predictions relevant to the hydrogenic case, the structure of the interference pattern evolves smoothly with the excess energy above the saddle point and is only weakly affected by the presence of continuum Stark resonances. In this paper, we describe a semiclassical analysis of this process and present numerical simulations in excellent agreement with the experimental results. It is shown that the background contribution dominates in the observations, as opposed to the behavior expected for hydrogenic systems where the interference pattern is qualitatively different on quasidiscrete Stark resonances.

I. INTRODUCTION

Though it was one of the first problems treated in the framework of quantum mechanics, the Stark effect of simple atoms is still topical both from the experimental and theoretical point of view (see, e.g., Refs. [1–3]). One of the major interests of the Stark effect is the possibility to produce quasidiscrete resonances, which are directly coupled to the ionization continuum. Not only does this particular feature allow the study of important types of dynamical behavior regarding the photoionization process itself, but, more interestingly from the point of view of the work presented here, a simple atomic system placed in an external electric field and excited in the region around the ionization threshold represents a prototypical atomic system with a large spatial extension that can be observed directly in the macroscopic world. In other words, the physical information contained in the outgoing flux of electrons produced in a photoionization experiment provides macroscopic information that can directly be related to the microscopic nature of the electron motion in the vicinity of the nucleus. This offers the opportunity to visualize, on a macroscopic scale, the intimate nature of the electronic wave function of an atomic system.

Recent developments in the field of photoelectron imaging have allowed the direct observation of the oscillatory structure of a wave function, first in the simple case of photodetachment [4] and more recently in the more complex case of photoionization [5]. This kind of photoelectron imaging is denoted as microscopy, since it introduces the capability of visualizing an electronic wave function (or more precisely: its square modulus) on a macroscopic scale. The principle of photodetachment and photoionization micros-

copy was initially introduced in the early 1980s by Demkov [6], Kondratovich and Ostrovsky [7–10]. These authors discussed the possibility of an experiment where the two-dimensional flux of electrons escaping from a photodetachment or photoionization process in the presence of an electric field could be measured using a position-sensitive detector located at a macroscopic distance. On the detector, the image formed by the electrons is the square modulus of the transverse component of the electronic wave function. Observed oscillatory patterns can be interpreted as a manifestation of interferences among various classical trajectories by which the electron moves from the atom to the plane of detection. In photodetachment, only two trajectories interfere at each detector position and the observed structures can easily be interpreted based on analytical expressions of the phase accumulated along both trajectories [6,7]. In the case of photoionization, the trajectories are considerably more complex [8,11,12] and one has to take into account the interference among an infinite number of classical paths. The simple parabolic trajectories relevant to the case of photodetachment are strongly perturbed, due to the Coulomb interaction between the ejected electron and the residual ion. Therefore, two-dimensional flux measurements are predicted to show a considerably more complex structure. As shown in Fig. 1, the combination of the Coulomb and Stark fields gives rise to the formation of a saddle point in the potential experienced by the electron, which lies at an energy

$$E_{sp} = -2\sqrt{F}. \tag{1}$$

The zero of the energy scale is defined as the field-free ionization limit. Here and in the following, we consider only ionization of neutral atoms, i.e., the residual charge of the ion is set to $Z = 1$. Except when explicitly specified, all formulas are given in atomic units. Above the saddle-point energy, the continuum is highly structured and exhibits quasidiscrete Stark resonances manifesting the presence of long-lived electron trajectories.

*Present address: Philips Electronics Nederland BV, Prof. Holstlaan 4, 5656 AA, Eindhoven, The Netherlands.
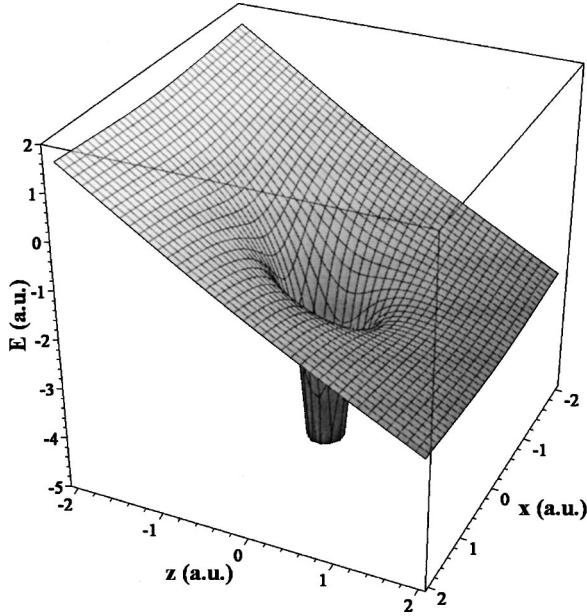
FIG. 1. Schematic view of the potential energy E resulting from the combination of the Coulomb and Stark fields in a field $F = 1$ a.u. (all quantities are given in atomic units). A saddle point at energy E_{sp} appears in the potential experienced by the Rydberg electron.

In this paper, we describe an analysis of the experimental results obtained recently in photoionization microscopy of xenon [5]. These results are analyzed within the framework of the semiclassical model described in a series of papers by Kondratovich and Ostrovsky [7–10]. However, as opposed to the hydrogenic development followed in these papers, we do not make any further approximations beyond the standard semiclassical description. More specifically, in order to account for the experimental observations, we will consider all classical trajectories and the phase (or reduced action) accumulated along these trajectories. In this process, we completely neglect tunneling integrals that do not correspond to any existent open classical trajectory. Furthermore, though the Stark spectrum is highly structured above E_{sp}, we will not apply any quantization conditions but will treat the entire energy domain of interest as a dense continuum. This assumption is supported by the high degree of mixing among all quasidiscrete Stark states and also by the finite width of every resonance in combination with the limited resolution of the excitation laser (typically 0.1 cm^{-1}). Replacing the Stark resonances by a simple continuum when evaluating the interference pattern will be further justified by the high degree of agreement observed between the experimental results and the simulations (see Sec. V). The excitation of a dense continuum contrasts with the case of a pure hydrogenic system where well-defined parabolic states are individually accessible with a fringe pattern that is a function of the quantization along coordinate ξ. In the xenon experiments, one of the most striking experimental features observed was the smooth evolution of the oscillatory structure as a function of the excess energy above the ionization threshold. We will show that this feature can be entirely accounted for by assuming an initially isotropic electron angular distribution. In

other words, instead of a well-structured atomic wave function at short range such as in atomic hydrogen, which is characterized by pure parabolic quantum numbers (n_1, n_2, m_ℓ) and a strong alignment of the electron wave packet with respect to the electric-field axis, the strong mixing among all parabolic states in a nonhydrogenic system has the consequence that the short-range wave function may approximately be described by a simple s wave without introducing significant errors in the final computational results.

In the following, our description will be limited to the region of negative energies above the saddle point for the sake of clarity, the present experimental results being limited to that region. However, the extension to the continuum at higher (positive) energies does not introduce any specific difficulty, and only minor modifications to the explicit formula given in the present paper are required.

II. CLASSICAL TRAJECTORIES

It is well known that the equations of the classical motion of an electron in the combination of a Coulomb attraction and a uniform electric field F directed along the z axis are separable in parabolic coordinates [14,15]:

$$\xi = r + z, \quad \eta = r - z, \quad \varphi = \tan^{-1}(y/x). \quad (2)$$

The classical problem of a hydrogen atom in an electric field is fully integrable and has exact analytical solutions. Beletzky [13] has extensively studied the nature of these solutions in the context of celestial mechanics. In quantum mechanics, exact numerical solutions may be obtained. However, the presence of an ionization continuum at any energy prevents the existence of analytical stationary solutions. The classical motion has been described thoroughly by Kondratovich and Ostrovsky in Ref. [8] and we have already analyzed this motion in the particular context of slow photoelectron imaging in Ref. [12]. In the following, we recall the main results of this analysis with emphasis on the case of negative energies. Explicit formulas relevant to the other domains of energy are available in Refs. [7–10] and [17–19]. We emphasize the nature of the classical trajectories and particularly the distinction between direct and indirect trajectories, which is of primary importance in the image and fringe pattern formation. Introducing the reduced time variable τ according to $d\tau = dt/r$, the equations of motion for an electron of total energy E in a static electric field F may be written as follows in atomic units:

$$\frac{d\xi}{d\tau} = 2\xi \left(\frac{E}{2} + \frac{Z_1}{\xi} - \frac{p_\phi^2}{4\xi^2} - \frac{F\xi}{4} \right)^{1/2},$$

$$\frac{d\eta}{d\tau} = 2\eta \left(\frac{E}{2} + \frac{Z_2}{\eta} - \frac{p_\phi^2}{4\eta^2} + \frac{F\eta}{4} \right)^{1/2}. \quad (3)$$

In the following, we describe only the planar motion characterized by a zero value of the projection of the orbital angular momentum p_ϕ on the field axis F. In fact, this simplification does not introduce any lack of generality, since the Coulomb field affects the trajectories at very large distances
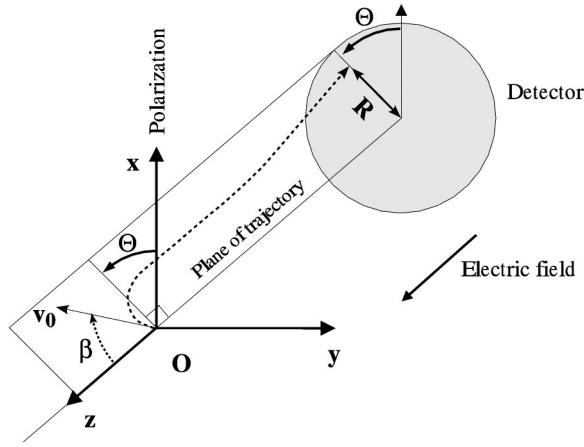
FIG. 2. Schematic view of the experimental arrangement used for photoionization microscopy. Photoionization occurs at point O. The electric field is oriented along the z axis, perpendicular to the detector. The laser polarization is oriented along the x axis. The angle Θ between the x axis and the plane of trajectory, and the angle β between the initial velocity $\bar{v}_0$ and the electric field are indicated.

(several microns) compared to atomic distances and the orbital angular momentum p_ϕ (similar to the magnetic quantum number m) does not significantly influence the electron motion in the present case. The separation constants Z_1 and Z_2 (where $Z_1 + Z_2 = 1$, the atomic charge of the ion core) are related to the ejection angle β between the initial velocity of the photoelectron and the electric field axis by

$$Z_1 = \cos^2(\beta/2) \quad \text{and} \quad Z_2 = \sin^2(\beta/2). \tag{4}$$

A schematic view of the experimental process, showing the relevant angles, is presented in Fig. 2. Integration of Eq. (3) gives the parabolic coordinates ξ and η as Jacobi elliptic functions of the reduced time variable τ. The general solutions are available in Ref. [8]. Below, we simply recapitulate the notations and results valid in the energy domain $E_{sp} \leq E \leq 0$ relevant to the experimental situation described here.

Let us first consider the motion along the ξ coordinate. Along this coordinate, the classical motion is periodic in τ and confined in the region $0 \leq \xi \leq \xi_{max}$ with the maximum value ξ_{max} defined as

$$\xi_{max} = \frac{|E|}{F}\left[\left(1 + \frac{Z_1}{Z_c}\right)^{1/2} + 1\right], \tag{5a}$$

where we have introduced the critical separation constant

$$Z_c = \frac{E^2}{4F}. \tag{5b}$$

The expression for the ξ coordinate of the electron is

$$\xi(\tau) = \frac{\xi_{max} sn^2(\varphi|m_\xi)}{m_\xi^{-1} - sn^2(\varphi|m_\xi)}, \tag{6a}$$

where the variable and argument of the elliptic sine function are defined, respectively, as

$$\varphi = \frac{1}{\sqrt{2}}\left(1 + \frac{Z_1}{Z_c}\right)^{1/4}\sqrt{-E}\,\tau, \quad m_\xi = \frac{1}{2}\left(1 - \frac{1}{\sqrt{1 + Z_1/Z_c}}\right). \tag{6b}$$

The nature of the motion along the η coordinate depends on the relative value of the separation constant Z_2 compared to the critical separation constant Z_c.

(i) For $Z_2 < Z_c$ (i.e., $E < -2\sqrt{Z_2 F}$), the electron motion is bound. An electron that is launched at an angle $\beta < \beta_c$—such that $E < -2\sqrt{Z_2 F}$—can never escape the attractive field of its ion, even though its energy lies above the saddle point. The critical angle β_c is

$$\beta_c = 2 \arcsin\left(\frac{-E}{2\sqrt{F}}\right). \tag{7}$$

(ii) For $Z_2 \geq Z_c$ (i.e., $0 \geq E \geq -2\sqrt{Z_2 F}$), the expression for the η coordinate of the electron is

$$\eta(\tau) = \eta_+\left(\frac{1 - cn(\Theta|m_\eta)}{sn(\Theta|m_\eta)}\right)^2, \tag{8a}$$

where

$$\eta_+ = \frac{|E|}{F}\left(\frac{Z_2}{Z_c}\right)^{1/2}, \tag{8b}$$

and the variable and argument of the elliptic functions are defined, respectively, as

$$\Theta = \left(\frac{Z_2}{Z_c}\right)^{1/4}\sqrt{-E}\,\tau, \quad m_\eta = \frac{1}{2}\left[1 + \left(\frac{Z_c}{Z_2}\right)^{1/2}\right]. \tag{8c}$$

Equation (8a) implies that the electron escapes to infinity when $sn(\Theta|m_\eta)$ vanishes, i.e., when $\Theta = 2\mathbf{K}(m_\eta)$, where $\mathbf{K}(m_\eta)$ is the complete elliptic integral of the first kind. Therefore, ejection of the electron to infinity corresponds to a reduced time given by $\tau = T_\eta$ with

$$T_\eta = 2\mathbf{K}(m_\eta)\left(\frac{Z_c}{Z_2}\right)^{1/4}(-E)^{-1/2}. \tag{9}$$

On the other hand, the motion along coordinate ξ described by Eq. (6a) is periodic in τ with a period T_ξ given by

$$T_\xi = 2\sqrt{2}\mathbf{K}(m_\xi)\left(1 + \frac{Z_1}{Z_c}\right)^{-1/4}(-E)^{-1/2}. \tag{10}$$

The number of zeros along coordinate ξ, i.e., the number of crossings of the electron trajectory with the z axis (field axis) during the motion of the electron from the force center to infinity (not counting the force center itself) is thus the integer part of the ratio T_η/T_ξ. One can find an infinite number of photoelectron trajectories passing through any point (ξ_0, η_0) in the classically accessible region. Following Kondratovich and Ostrovsky [8], these trajectories are classified according to the number N of oscillations along ξ, where N is defined as the number of maxima appearing in $\xi(\tau)$. Furthermore, trajectories are labeled "+" or "−", de-
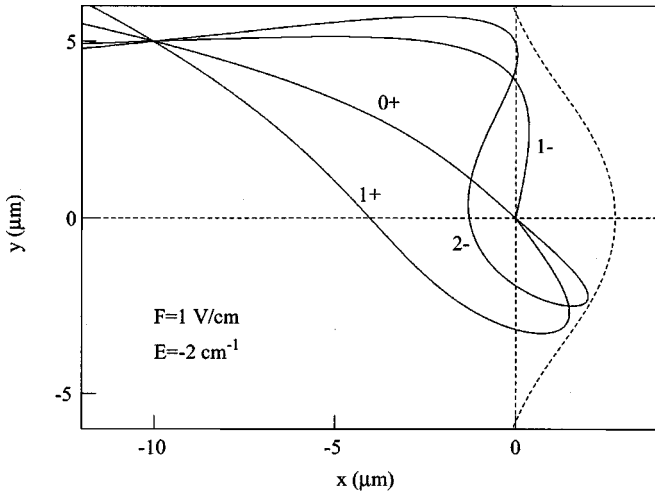
FIG. 3. Examples of trajectories in a field $F=1$ V/cm at an energy $E=-2$ cm^{-1}. In that case, since the energy lies above the onset of direct trajectories at $E_{dir}\approx-4.73$ cm^{-1}, the direct trajectories 0^+ and 1^- are allowed.

pending on whether the number of zeros along $\xi(\tau)$ is equal to N or $N-1$. For $N=0$, only the 0^+ trajectory exists. These basic properties of the electron trajectories are exemplified in Fig. 3. From the point of view of the formation of the image, this classification of the trajectories is extremely important as it defines the distinction between direct trajectories and indirect trajectories introduced in our previous papers. Direct trajectories correspond to the case where the electron is ejected approximately in the direction of the detector without crossing of the z axis (no zeros in ξ). These direct trajectories are not unlike the trajectories which occur in the case of $Z=0$ (photodetachment), where the electron follows a parabolic trajectory to the plane of detection. By contrast, indirect trajectories correspond to the case where the electron is scattered by the core and crosses the z axis at least once (i.e., one or several zeros in ξ). Hence, in photoionization ($Z=1$), low-energy photoelectrons will contribute to one of two distinct concentric structures depending on the direction of the electron emission, namely, an inner structure corresponding to electrons ejected down field towards the hole in the Coulomb+dc electric-field potential (direct ionization) and an outer one corresponding to electrons ejected away from the hole, which only ionize following further interactions with the ionic core (indirect ionization). Recently, we published the experimental observation of this phenomenon [20] in imaging of the photoionization of atomic xenon. The observed images exhibited an outer ring, corresponding to the indirect ionization process, and an inner ring corresponding to the direct ionization process, and clearly revealed how the indirect process dominates at threshold whereas the direct process dominates at higher excitation energies and above the field-free ionization limit. Therefore, direct trajectories build up the central part of the image with a radius R_I (see Fig. 4), while indirect trajectories also contribute to the external part of the image up to a radius R_{max}^c given by

$$R_{max}^c=\left(\frac{E}{F}+\frac{2}{\sqrt{F}}\right)^{1/2}(\sqrt{2L})=\left[2L\left(\frac{E-E_{sp}}{F}\right)\right]^{1/2}, \quad (11)$$
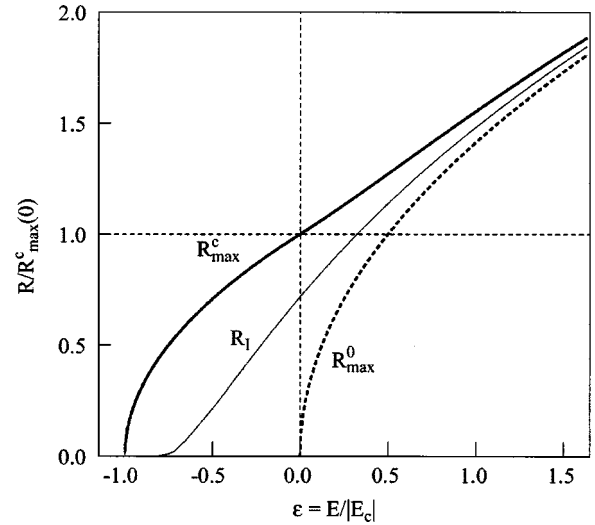

FIG. 4. Maximum radius of impact neglecting the Coulomb term R_{max}^0 (dotted line) and taking the Coulomb term into account, R_{max}^C (broad solid line), as a function of the reduced energy ε. At large ε values, R_{max}^0 and R_{max}^C do not differ significantly, while for $-1\leqslant\varepsilon\leqslant1$ the effect of the Coulomb interaction cannot be neglected. The radius R_I represents the maximum radius of impact for direct trajectories that never cross the field axis.

where L is the distance between the force center and the detector. According to the notation introduced above, direct trajectories are denoted 0^+ and 1^-. All other trajectories are indirect. The variation of the radius of impact R on the detector as a function of the ejection angle β and the connection of the $N^\pm$ index of the trajectory is illustrated in Fig. 5. There are an infinite number of indirect trajectories reaching each accessible point on the detector. However, the relative importance of each of these trajectories depends on the electric-field strength and on the energy of the outgoing electron. For example, just below $E=0$ most trajectories are direct, while just above the saddle point all trajectories are indirect. The distinction between direct and indirect trajectories allows introducing an energy threshold E_{dir} that corresponds to the onset of direct trajectories. Below E_{dir} no direct
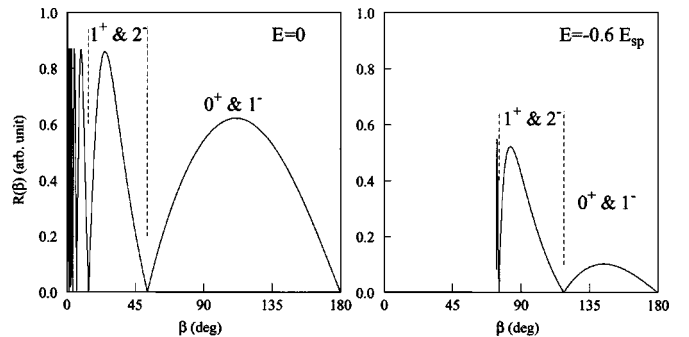

FIG. 5. Typical examples of the variation of the radius of impact $R(E,F,\beta)$ as a function of the ejection angle. The N index of the trajectory relevant to the corresponding region of space is indicated. Left: $E=0$, all trajectories are open irrespective of angle β. Right: $E=0.6E_{sp}$, electrons launched at an angle β smaller than the critical angle β_c [Eq. (7)] can never escape the Coulomb attraction.

trajectories are allowed for any ejection angle β, while above E_{dir} trajectories 0^+ and 1^- exist for a limited range of ejection angles. The limit of vanishing direct trajectories corresponds to the case where $T_\xi = T_\eta$ when $Z_1 \rightarrow 0$. Combining Eqs. (6c) and (8c) giving the arguments of the Jacobi elliptic function and Eqs. (9) and (10) for the period along both coordinates, one finds in the end,

$$E_{dir} = \kappa E_{sp}, \tag{12}$$

with κ being the solution of

$$\sqrt{2} \mathbf{K}(\tfrac{1}{2} + \tfrac{1}{2}\kappa) \sqrt{\kappa} = \pi. \tag{13}$$

The constant $\kappa = E_{dir}/E_{sp}$ is $\approx 0.775\,156\,372\,63...$. Note that this threshold energy E_{dir}, used in our previous paper [5], is determined here exactly. Although of less general importance than the saddle-point energy, it is another remarkable value since the qualitative appearance of the image is radically modified at this energy. Indeed, just above E_{dir}, direct trajectories appear in the center of the image as a very intense spot, as if the corresponding electrons were focused by the bottleneck in the Coulomb+dc field potential surface.

In summary, the analysis of classical trajectories allows to distinguish four regions of energy: (1) below the saddle-point energy ($E < E_{sp}$), the electron motion is bound; (2) for $E_{sp} \leqslant E < E_{dir}$, only indirect trajectories are allowed, which exhibit at least one crossing of the z axis; (3) for $E_{dir} \leqslant E < 0$, direct and indirect trajectories coexist; (4) for $0 \leqslant E$, the motion is always open along the η coordinate.
In cases (2) and (3) that are considered here, the motion is bound along ξ; it is bound along η if $\beta < \beta_c$, and open along η if $\beta \geqslant \beta_c$.

Note that the topology of the electron trajectories, and hence the pattern of impacts at large distance, depends only on the dimensionless parameter introduced in Eq. (5b), $Z_c = \varepsilon^2$, with the reduced energy $\varepsilon = E/E_{sp}$. The parameter Z_c (or equivalently ε) is thus a measure of the relative strength of the Coulomb and Stark fields.

A remarkable aspect of threshold photoionization is that the radius of the image evolves rather differently when the Coulomb field is taken into account. While it is exactly proportional to $F^{-1/2}$ when neglecting the Coulomb field (as is the case in photodetachment), it is approximately proportional to $F^{-1/4}$ in the region between the saddle-point energy and the zero-field-ionization threshold. For example, at $E = 0$, Eq. (11) gives exactly $R_{max}^c = 2^{1/2} F^{-1/4} (2L)^{1/2}$. This distinction is essential in photoionization microscopy. The evolution of the overall features observed, in particular, the size of the distribution of impacts, does not evolve linearly with $F^{-1/2}$ but it is proportional to $F^{-1/4}$. As a consequence, the evolution of the image dimension as a function of the Stark field magnitude is extremely slow as compared to the case where the Coulomb field may be neglected.

III. ACCUMULATED PHASE AND SEMICLASSICAL WAVE FUNCTION

As mentioned in the preceding section, the problem of a hydrogenic atom in a uniform electric field F oriented along the z axis is separable in parabolic coordinates [Eq. (2)]. Following the usual notations [14,15], the eigenfunction may be written as

$$\Psi(\xi, \eta, \varphi) = (2\pi\xi\eta)^{-1/2} \chi_1(\xi)\chi_2(\eta) \exp(im\varphi), \tag{14}$$

with the functions χ_1 and χ_2 solutions of the ordinary differential equations:

$$\frac{d^2\chi_1}{d\xi^2} + \left(\frac{E}{2} + \frac{Z_1}{\xi} - \frac{m^2 - 1}{4\xi^2} - \frac{1}{4} F\xi \right) \chi_1 = 0, \tag{15a}$$

$$\frac{d^2\chi_2}{d\eta^2} + \left(\frac{E}{2} + \frac{Z_2}{\eta} - \frac{m^2 - 1}{4\eta^2} + \frac{1}{4} F\eta \right) \chi_2 = 0, \tag{15b}$$

where m is the magnetic quantum number, and Z_1 and Z_2 are separation constants satisfying $Z_1 + Z_2 = 1$ [see Eq. (4)]. Similar to the classical equations of motion, Eq. (15a) implies that the motion along the ξ coordinate is always finite. However, it is not pertinent at this point to apply any quantization connecting Z_1 to the energy E, which would be relevant in the case of atomic hydrogen. Based on the discussion in the preceding section, the spectrum above the saddle point E_{sp} in a nonhydrogenic atom (as described in the following) is treated as a true continuum and we do not consider the case of resonances in the final state.

In the discussion of the classical motion, we focused on the case of the planar motion with $m = 0$. The same restriction will apply in our presentation of the semiclassical description, i.e., we neglect the centrifugal term in the electron energy and consider only the case $m = 0$. We introduce modified momenta [21] along ξ and η coordinates (respectively, p_ξ and p_η) as follows:

$$\tilde{p}_\xi = \left(\frac{E}{2} + \frac{Z_1}{\xi} - \frac{F\xi}{4} \right)^{1/2},$$

$$\tilde{p}_\eta = \left(\frac{E}{2} + \frac{Z_2}{\eta} + \frac{F\eta}{4} \right)^{1/2}. \tag{16}$$

Following the description in the preceding section, there exist in the case of unbound motion ($E_{sp} \leqslant E$ and $Z_2 \geqslant Z_c$) an infinite number of photoelectron trajectories passing via any point $M(\xi_0, \eta_0)$ in the classically accessible region. In the semiclassical approximation, the photoelectron wave function at this given point $M(\xi_0, \eta_0)$ may be represented as a sum of the contributions from all trajectories leading from the electron source to the point M as

$$\Psi(M) = \sum_{N=0}^{\infty} \chi_{N^+} \exp(iS_{N^+}) + \sum_{N=1}^{\infty} \chi_{N^-} \exp(iS_{N^-}), \tag{17}$$

where χ_{N^+} and χ_{N^-} are slowly varying functions which depend on the separation constant Z_1 (or equivalently on the ejection angle β) and on the angle θ. The function $\chi_{N^\pm} = \chi(\beta, \theta)$ represents the "weight of a given trajectory." Its precise determination supposes a full quantum description of the problem and is therefore not attainable here. A develop-

ment on partial ℓ waves is introduced below [Eq. (23)]. It will be restricted to s wave in a first step. The quantity $S_{N\pm}$ is the action along the classical trajectories $N^\pm$, where as before N is the number of turning points between the origin and the point M, the superscript $+$ corresponds to the case where the number of z-axis crossings equals N, while the superscirpt $-$ is is relevant to trajectories where this number is $N-1$. The total action may be expressed as the sum of contributions of the momentum along the ξ and η coordinates, respectively,

$$S_{N^+} = \int_0^{\eta_0} \tilde{p}_\eta(Z_2,E)d\eta + 2NS_\xi + \int_0^{\xi_0} \tilde{p}_\xi(Z_1,E)d\xi,$$

(18a)

$$S_{N^-} = \int_0^{\eta_0} \tilde{p}_\eta(Z_2,E)d\eta + 2NS_\xi - \int_0^{\xi_0} \tilde{p}_\xi(Z_1,E)d\xi,$$

(18b)

with

$$S_\xi = \int_0^{\xi_{\max}} \tilde{p}_\xi(Z_1,E)d\xi,$$

(19)

where $\xi_{\max}$ is the ξ coordinate of the turning point defined in Eq. (5). The total action contains two terms related to parabolic coordinate ξ, namely, one that takes into account the number of complete oscillations in the ξ coordinate performed by the electron trajectory, and one taking into account the accumulated phase from the last axis crossing of the trajectory until the arrival at the detector. The explicit expressions of the phase integrals introduced in Eq. (18) are given as elliptic integrals of hypergeometric functions in the papers of Kondratovich and Ostrovsky [7,16] and in a more general although less handy form in Harmin [17–19]. Their expressions restricted to the region of interest between the saddle-point and the zero-field-ionization energies are reproduced below for completeness.

The phase integral S_ξ for the motion along the ξ coordinate defined in Eq. (18) is finite and may be expressed as a function of the hypergeometric function as

$$S_\xi(Z_1,E,F) = \frac{\pi Z_1^{3/4} \tau^{1/4}}{\sqrt{2} F^{1/4}} \mathbf{F}(-\tfrac{1}{2},\tfrac{1}{2},2;-\tau),$$

(20a)

with $\mathbf{F}$ the hypergeometric function [22] and the parameter τ given by

$$\tau = \frac{(E^2+4Z_1F)^{1/2}+E}{(E^2+4Z_1F)^{1/2}-E}.$$

(20b)

On the other hand, the phase integral S_η for the motion along the η coordinate is arbitrarily large as η tends towards infinity (macroscopic value). Consequently, rather than the absolute phase, one has to evaluate the relative phase shift S_η^0, being the difference between S_η and the diverging part of the integrals S_0 with

$$S_\eta(Z_2,E,F) = \int_0^{\eta_0} \tilde{p}_\eta(Z_2,E)d\eta = \int_0^{\eta_0} \left[\frac{E}{2} + \frac{Z_2}{\eta} + \frac{F\eta}{4} \right]^{1/2} d\eta$$

(21a)

and

$$S_0(E,F) = \int_0^{\eta_0} \left[\frac{E}{2} + \frac{F\eta}{4} \right]^{1/2} d\eta.$$

(21b)

According to Harmin, it follows that above the saddle-point energy ($Z_2 \geqslant Z_c$),

$$S_\eta^0(Z_1,E,F) = S_\eta - S_0$$

$$= \frac{2^{3/2} \pi Z_2^{3/4}}{F^{1/4}} \frac{x^{1/2}}{(1+x)^{3/2}} \mathbf{F}\left(-\frac{1}{2}, \frac{1}{2}, 2; \frac{-1}{x} \right),$$

(22a)

with

$$x = \frac{2(Z_2F)^{1/2}+E}{2(Z_2F)^{1/2}-E}.$$

(22b)

Compared to the case of photodetachment, where the equation of motion and the phase integrals are trivial expressions of the electron energy and external field, there does not exist in the present case an obvious analytical form in terms of which the photoelectron trajectories and the accumulated phase shift can be discussed. As a consequence, it is not possible to express simply in a compact form general scaling laws governing the evolution of the observable features as a function of the electron energy E and the external static field F. Therefore, in the following section some selected examples of simulations and comparisons with a limited number of experimental results are described.

The wave function [Eq. (17)] at an arbitrary point on a plane detector located at distance L from the origin depends both on the reduced action $S_{N\pm}$ and on the functions $\chi_{N\pm} = \chi(\beta,\theta)$ introduced above. In this paper, we chose somewhat arbitrarily the expression of the function χ by expanding this quantity in terms of partial ℓ waves such that

$$\chi = \sum_{\ell m} C_{N\pm}^{\ell m} Y_\ell^m(\theta,\varphi).$$

(23)

Since the semiclassical model does not allow to evaluate this function, we will restrict our examples to the simplest case of an s wave where the summation in Eq. (23) is restricted to the term $\ell=0$. In other words, we will give only examples corresponding to an isotropic initial distribution of trajectories. Attributing the same weight to every trajectory is, of course, the main approximation made in the present simulation. However, this approximation is rather realistic, since a Stark resonance in the continuum of a nonhydrogenic atom consists of a mixture of a large number of parabolic eigenstates and is less localized than the equivalent in hydrogen. Furthermore, this approximation will be supported by a comparison with the experimental results that clearly exhibit a limited dependence of the intensity on the angle θ (that has

no influence on the interference pattern) with respect to the polarization axis of the excitation laser and a smooth dependence on the ejection angle β with respect to the electric-field axis. The dependence on β changes only the relative intensity of the various fringes but has a negligible influence on their position. In addition and to the same order of approximation, we arbitrarily set the initial phase at the core ($r=0$) to a constant value for all electron ejection angles, so that Eq. (18) may be used as is to compute the relative phase at the detector.

The procedure for the calculation is thus as follows. For a given energy E, a given electric-field value F, and a given distance L between the origin where the photoionization takes place and the observation plane, we calculate first the radius of impact as a function of the ejection angle $R(\beta)$ according to Eqs. (5)–(8). Typical examples are presented in Fig. 5 together with the N index of the trajectory relevant to the corresponding region of space. Next, the reduced action S along the trajectories is calculated according to Eqs. (18)–(22). Next, the final contribution of a classical trajectory launched at a given angle β to $\Psi(M)$ is weighted according to the density of trajectories corresponding to that angle. Both the wave function [Eq. (17)] and the electron flux, which is proportional to the square modulus of the wave function, may be expressed either in angular coordinates (β,θ) or in the laboratory polar coordinates (R,θ) corresponding to the position on the plane detector. Here we note that—when using angular coordinates—we prefer to use the ejection angle β rather than the azimuthal angle ϕ, since it is most relevant to the electron motion. The electron flux I may be expressed in both coordinate systems according to the relation

$$I_\beta(\beta,\theta)S_{\beta\theta}=I_R(R,\theta)S_{R\theta}, \tag{24}$$

where $S_{\beta\theta}=L^2\sin\beta\,d\beta\,d\theta$ and $S_{R\theta}=R\,dR\,d\theta$ are the corresponding elementary surfaces. After transformation from the atomic angular frame to laboratory polar coordinates, one obtains for the partial amplitude χ in the detector frame,

$$\chi_R(R,\theta)=\left(\frac{\sin\beta}{R\dfrac{dR}{d\beta}}\right)^{1/2}L\chi_\beta(\beta,\theta). \tag{25}$$

The resulting wave function $\Psi(M)$ at point $M(R,\theta)$ is subsequently obtained by summing the amplitude over all possible trajectories according to

$$\Psi(M(R,\theta))=\sum_i\left[\chi(\beta_i,\theta)(\sin\beta_i\,d\beta_i)/(R\,dR)\right]^{1/2}$$
$$\times\exp\{i[S_\xi(\beta_i)+S_\eta(\beta_i)]\}, \tag{26}$$

where β_i represent all ejection angles leading to the detection of the electron at radius R. The calculated radial probability distribution $P_{\mathrm{calc}}(R)$ is then obtained according to

$$P_{\mathrm{calc}}(R)=R\int|\Psi(M(R,\theta))|^2d\theta. \tag{27a}$$

This distribution is to be compared with the experimental radial probability distribution $P_{\mathrm{expt}}(R)$ defined as

$$P_{\mathrm{expt}}(R)=R\int P(R,\theta)d\theta, \tag{27b}$$

where $P(R,\theta)$ represents the intensity distribution in the image in polar coordinates R and θ.

IV. SIMULATIONS

The aim of the present section is to compare the results of the simulations based on the semiclassical model described above with experimental results obtained in the photoionization of xenon [5]. The experimental results show unambiguously that in a nonhydrogenic system such as xenon, the evolution of the interference pattern is a smooth function of the energy E. The number of dark fringes increases smoothly from zero at the saddle point to large, but finite, values in the region of the open continuum. Here, our purpose is not to describe extensively these experimental results, which will be done in another paper. Rather, we will show that the major experimental observations may be fully interpreted within the semiclassical framework with a high degree of accuracy. The main experimental observations are essentially the following:

(1) In photoionization, a clear oscillatory pattern is visible in the high-resolution electron image that is observed above a single-ionization threshold.

(2) The number of dark fringes in this oscillatory pattern increases smoothly with the excess energy above the saddle point and is apparently independent of whether the excitation is on or off a large resonance although the overall intensity and some details of the pattern depend on the resonant character of the excitation process.

Regarding the second point above, it is obvious that a simulation based on the semiclassical model described in the previous sections assuming an isotropic distribution of the initial electron trajectories will necessarily lead to a smooth evolution as a function of the energy. As a consequence, the agreement between experiment and model from this point of view will simply validate the assumption relative to the initial distribution without giving the quantitative explanation that must necessarily rely on a full quantum calculation.

Let us first consider the general evolution of the interference pattern predicted according to the description presented above. First, the evolution of the interference pattern as a function of the field magnitude will be discussed at the zero-field-ionization threshold $E=0$. This evolution is presented in Fig. 6, where the radial distribution $f(R)$ has been plotted for various realistic electric-field strengths from 10^{-8} to 10^{-4} a.u. (one atomic unit of electric field is 5.14×10^9 V/cm). Note that the simulations are performed using a field F that persists all the way to the plane of detection, whereas the experiment involves a field-free region. The effect of this field-free region is merely to magnify the size of the image, without affecting the interference pattern itself. The size of the images shown in Fig. 6 is extremely small. For instance, at $E=0$, with a photoelectron spectrometer half
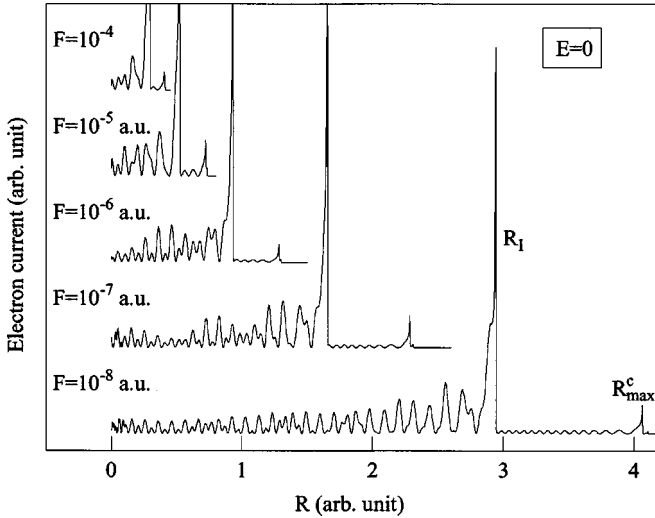
FIG. 6. Radial distribution of the electron current $f(R)$ at energy $E=0$ for various electric fields ranging from 10^{-8} to 10^{-4} a.u. (1 a.u. of electric field is $\approx 5.14 \times 10^9$ V/cm). The maximum radius of impact, R^c_{max}, as well as the radius of the direct component R_l, are indicated for the lowest-field value.

a meter long, the overall diameter of the image is about 100 μm at $F=10^{-4}$ a.u. and 1 mm at $F=10^{-8}$ a.u. The number of dark fringes is, respectively, 5 and 50 under these conditions. From Eqs. (18)–(22), it follows that for $E=0$, the quantity $SF^{1/4}$ is a constant. Combined with the fact that $R(\beta)F^{1/4}$ is a constant for $E=0$, we can expect a quasiconstant fringe spacing which depends only on the geometry of the spectrometer, and which is in the range 15–30 μm in Fig. 6. Taking into account the typical resolution of position-sensitive detectors (roughly 50 μm) and the finite spatial extension of the interaction region where the excitation laser and the atomic beam overlap, such structures are absolutely not visible without some modification of the imaging experiment. It is necessary to use some electron optics in the spectrometer in order (1) to compensate for the initial extension of the interaction region that is a strict limitation if a homogeneous electric field is used and (2) to magnify the geometrical pattern in order to resolve the detailed structure of the image by rendering the fringe spacing larger than the intrinsic resolution of the detector. Using the velocity-map imaging geometry [23], it is possible to solve the first limitation and to project electrons with a unique initial velocity vector originating from a source volume of about 1 mm to a single spot with a diameter smaller than 10 μm. Of course, when using velocity-map imaging, the electric field in the extraction region is not homogeneous over the entire volume of the spectrometer, but it may be assumed approximately constant over the small interaction region. However, the electric-field strength in the extraction region is no longer connected in a simple way to the various voltages applied on the spectrometer electrodes. As a consequence, the electric-field value must be estimated from the observed Stark spectrum (using the field dependence of the linear Stark effect) or the electric-field value can be derived from the image itself, as we will see in the following section. It turns out that the adjustment of the calculated and experimental images is ex-

tremely sensitive and this method has been used to refine the effective electric-field value. To solve the second limitation, we have developed an electrostatic magnifying lens that allows a magnification of the image on the detector by a factor as large as 20 without deterioration of the image quality, and above all without perturbation of the pattern of the interferogram [24]. With this magnifying lens, images can be recorded with a radius of several millimeters in a kinetic-energy domain and dc electric-field regime where (a) the number of fringes is not too high, and (b) the continuum Stark structure can be resolved. Due to our limited laser bandwidth (0.07 cm^{-1} in the visible, i.e., 0.14 cm^{-1} after frequency doubling), condition (b) was fulfilled only for $F > 500$ V/cm. However, working at a smaller field and a potentially larger image radius allowed us to obtain sharper images even though, in that case, the respective contribution of the continuum and of the resonances was more difficult to distinguish.

A couple of remarkable aspects that were already mentioned in the preceding section are visible in Fig. 6. First, the image size only changes very slowly as a function of the electric-field value. Indeed, at $E=0$ the maximum radius R^c_{max} is proportional to $F^{1/4}$ and going from a moderate field of 10^{-8} a.u. (about 50 V/cm) to a very large field of 10^{-4} a.u. (about 500 kV/cm) merely divides the image diameter by a factor of 10. Second, the fringe spacing is almost independent of the field value owing to the fact that the reduced action $S(\beta)$ scales as $F^{1/4}$. From a purely experimental point of view, this means simply (and rather counter-intuitively) that the interference pattern will be more easily resolved at a very high-field value where the low number of fringes combined with the lens magnification allows full resolution of the image. A low-field value of a few V/cm implies about 100 dark fringes at $E=0$, which is absolutely impossible to image with available detectors, while furthermore high-resolution velocity-map imaging becomes experimentally more challenging at low electric-field strengths, where loss of resolution due to small stray magnetic fields becomes a factor. On the contrary, working in the field range $F \approx 500–1000$ V/cm will simultaneously allow us to resolve the Stark spectrum in the energy domain, and the fringe pattern in the geometrical domain.

Figure 7 presents a series of simulations of radial distributions at $F=10^{-6}$ a.u. and at a range of excitation energies between $E=E_{sp}$ and $E=0$. The evolution of the indirect (outermost) contribution peaking at $R=R^c_{max}$ and the direct (innermost) contribution appearing at $E \geq E_{dir} \approx 0.77E_{sp}$, and peaking at $R=R_l$ is clearly distinguished. Furthermore, the development of the fringe pattern in the radial distribution is clearly observed. Note that, even though no simple scaling law can be derived for the evolution of the fringe spacing, except at $E=0$, where it is approximately constant as a function of the electric field, the distance between two dark fringes slowly decreases as the excess energy increases. Note also that the periodicity is roughly the same in the central part of the image ($R<R_l$) where both direct and indirect trajectories contribute, and in the external part ($R_l<R<R^c_{max}$) where only indirect trajectories are contributing. The
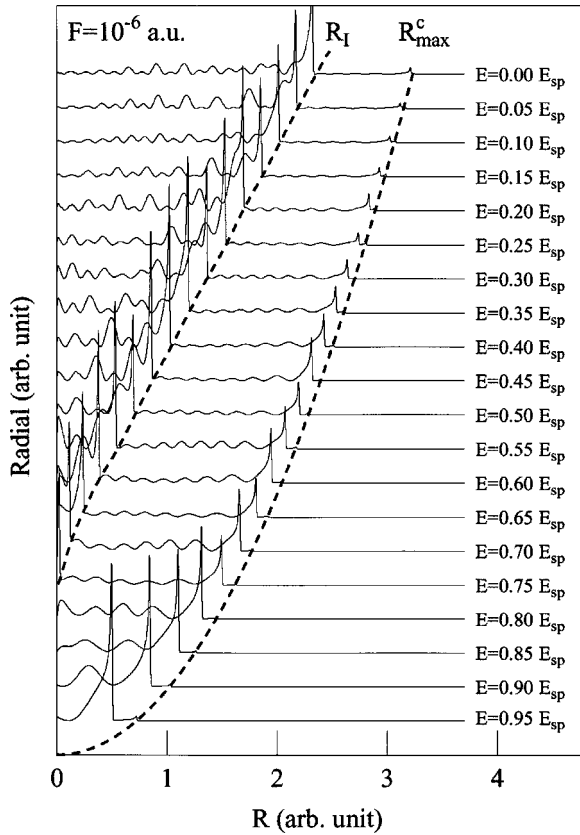
FIG. 7. Radial distribution of the electron current $f(R)$ at various energies between saddle point E_{sp} and $E=0$ in an electric field $F=10^{-6}$ a.u. (thin solid lines). The evolution of the maximum radius of impact R^c_{max} and of the radius of the direct component R_I as a function of the energy are plotted in broad dotted lines.
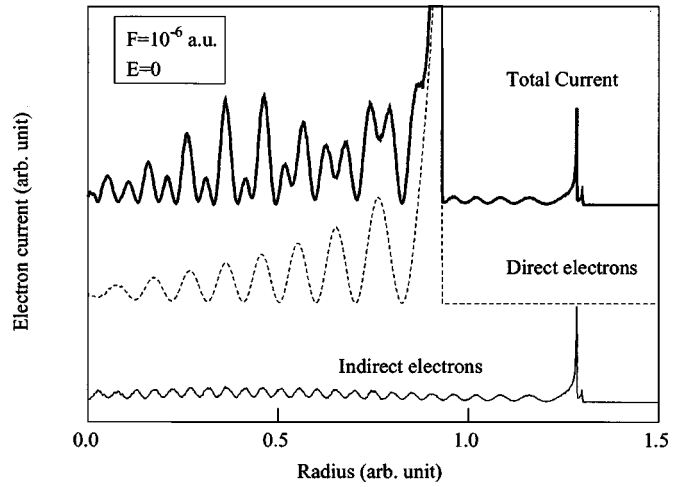

FIG. 8. Decomposition of the radial distribution of the photoelectron current $f(R)$ in its direct and indirect contributions at $E=0$ and $F=10^{-6}$ a.u. Bottom: square of the amplitude of the indirect electrons' contribution. Middle: square of the amplitude of the direct electrons' contribution. Top: total photoelectron current resulting from the combination of both amplitudes.

buildingup of the interference structure is more clearly seen in Fig. 8 where we have decomposed the total radial distribution in its direct and indirect components. This is achieved by calculating the square modulus of the amplitude by restricting the domain of ejection angles to the appropriate region. Direct and indirect trajectories lead to two completely different structures with noticeably smaller fringe spacing in the indirect component. In the inner region of the image, the regular patterns of the direct and indirect components give rise to a beating pattern and to a strong modulation of the dominant direct electron signal by the weaker electron signal corresponding to the indirect trajectories, which has a higher spatial frequency.

In conclusion, the most striking results of these simulations, based on the assumption of an isotropic initial distribution, are the following: (1) just above the saddle-point energy and below the onset of direct trajectories ($E_{sp} \lesssim E \lesssim E_{dir}$), the interference pattern is regular and evolves smoothly as a function of the excess energy, (2) as soon as direct trajectories are allowed ($E > E_{dir}$) a second intense pattern appears, at a lower spatial frequency, and a beating between the two patterns is visible in the radial distribution. Qualitatively, these two observations are in complete agreement with our experimental results (see the following section).

We note that the semiclassical approximation fails when the momentum vanishes somewhere along the trajectory. This is the case for trajectories that reach a local maximum in the radius [either R_I for direct trajectories or R^c_{max} for indirect trajectories, see Eq. (25)]. As a consequence, the simulations are invalid in the extreme outer part of the image corresponding to the indirect component and at the outer part of the contribution corresponding to the direct component. At these points the present simulation diverges, while a treatment taking properly into account the quantum nature of the problem and the contributions due to tunneling integrals would smooth out the pattern in these regions. However, the difference between our semiclassical description and an exact quantum description is expected to be substantial only in these very limited regions of the image and does not affect the overall structure of the image.

V. COMPARISON WITH SOME EXPERIMENTAL RESULTS

As described in previous Refs. [5,20], the present experimental results are obtained in the imaging of photoionization of metastable ($6s[\frac{3}{2}]_{J=2}$) xenon atoms produced in a standard electron-impact source. The experimental results compared to the semiclassical model in this paper were obtained when the metastable atoms were one-photon excited above the ionization threshold by means of a frequency-doubled tunable dye laser in the near UV [Nd:YAG (yttrium aluminum garnet) pumped Quanta-Ray PDL-3, with a 0.07 cm^{-1} bandwidth in the visible]. The laser polarization was set parallel to the plane of the detector. In usual velocity-map imaging experiments, this constraint of having the laser polarization in a plane parallel to the detection plane is required in order to be able to retrieve the three-dimensional velocity distribution from the image. The laser polarization is chosen as the vertical axis in Figs. 9–11. However, perpendicular
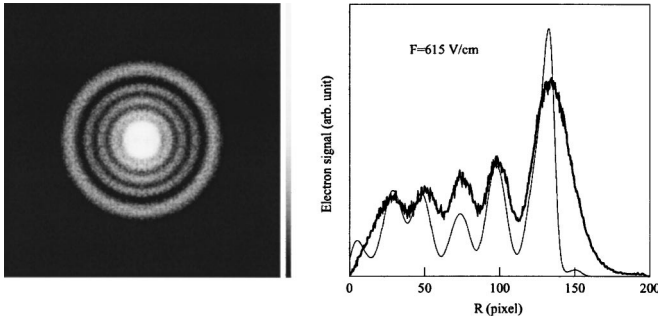
FIG. 9. Left: experimental photoelectron image recorded in a dc electric field of 615 V/cm, by exciting metastable Xe $6s[\frac{3}{2}]_{J=2}$ 23.8 cm^{-1} above the saddle point with a tunable ultraviolet laser polarized parallel to the plane of the detector, and along the vertical axis. Right: comparison of the experimental (broad solid line) and theoretical (thin solid line) radial probability distributions $f(R)$ of the image.

FIG. 11. Experimental photoelectron image recorded in a dc electric field of 615 V/cm, by exciting metastable Xe $6s[\frac{3}{2}]_{J=2}$ 46.3 cm^{-1} above the saddle-point energy. The central part of the image is dominated by direct trajectories. The outer part (spilling out of the detector), which is almost too weak to be seen on this scale, corresponds to indirect trajectories. Interferences between direct and indirect trajectories are revealed in the central part of the image by irregularities in the fringe pattern.

polarization may be chosen to use different selection rules. These observations in perpendicular polarization will be described in a forthcoming experimental paper. The excitation occurs in the extraction region of a velocity-map imaging spectrometer equipped with a magnifying lens required to visualize the interference pattern as described in Ref. [24].

Figure 9 shows a typical experimental image recorded at a field strength of 615 V/cm and with the laser tuned about 23.8 cm^{-1} ($E = -128.0$ cm^{-1}) above the saddle-point energy. The interference pattern is clearly observed, and five distinct bright fringes corresponding to constructive interference are visible. The radial probability distribution $P_{\text{expt}}(R)$, derived from the image using the procedure outlined, is compared with the simulation performed along the procedure described above. In contrast with the preceding section, the simulation results presented in this section have been smoothened in order to take into account the limited experimental resolution and to reduce the influence of the sin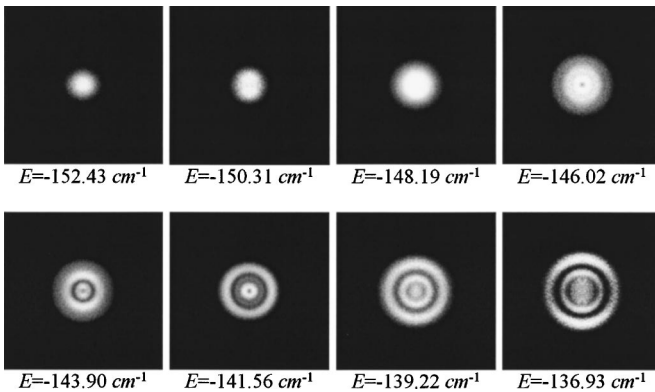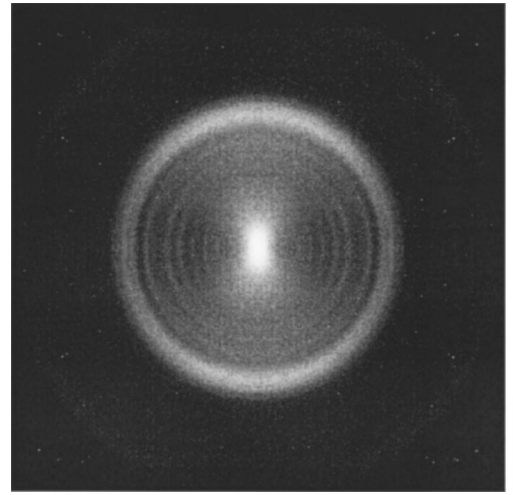gularities in the semiclassical calculations, which were discussed in the preceding section. A series of images were recorded similar to Fig. 9, while scanning the ionization laser frequency between the saddle-point and the zero-field-ionization threshold at field strengths of 615 V/cm allowing measurements both on pronounced quasidiscrete Stark resonances and between them. A number of representative images are shown in Fig. 10. As already mentioned, one of the most striking results of these measurements is the smooth evolution of the interference pattern when the energy increases. In the entire excitation range, the number of dark fringes increases smoothly as a function of the excess energy and—to a first approximation—the quasidiscrete Stark resonances only affect the amplitude of the modulation of the various fringes, but not the fringe position. This is underscored by the fact that the images in Fig. 10 were selected on the basis of the appearance of the excitation spectrum that suggested that these images result from excitation to eight neighboring members of one single Stark manifold or of overlapping manifolds. Indeed in this energy range, well above the Inglis-Teller limit, various manifolds corresponding to successive principal quantum numbers n are overlapping and, except the azimuthal quantum number m_l strictly controlled by selection rules, no precise quantum number may be defined. Nevertheless, from Fig. 10 it is abundantly clear that the number of fringes observed in the experiment is not at all related to the approximate transverse parabolic quantum number of a particular Stark state, but are determined by the energy with respect to the saddle point. Angular distributions observed in the experimental images will be described elsewhere, since they cannot be interpreted within the semiclassical model.

FIG. 10. Photoelectron images recorded on resonances at $F = 615$ V/cm. The energy increases from left to right. First image at $E = -152.43$ cm^{-1} is taken 0.6 cm^{-1} below $E_{\text{sp}} \approx -151.8$ cm^{-1} and corresponds to the case where photoionization occurs via tunneling, which is not accounted for by our semiclassical description. Other images are recorded between 1.5 and 14.9 cm^{-1} above E_{sp}.

The image presented in Fig. 9 is typical of the observa-

tions at energies below E_{dir}. Above E_{dir} the appearance of the image is qualitatively different and contains an intense central portion, which corresponds to direct ionization, surrounded by a weaker portion, due to indirect ionization. This is clearly visible in the image presented in Fig. 11, which is similar to Fig. 9 except that the energy now is 46.3 cm^{-1} ($E=-105.5$ cm^{-1}) above the saddle-point energy. Qualitatively, the interference in the inner region looks considerably more complicated: several of the interference rings are very intense, whereas others seem to be missing. As discussed in the preceding section, in the inner region the radial periods of the interference structures corresponding to the direct and the indirect path are incommensurate and a beat pattern occurs, where the interference at some radii is enhanced, while at other radii the two contributions partially cancel each other.

In Fig. 12, a series of experimental radial distributions are compared with the corresponding semiclassical simulations. The laser wavelength is calibrated absolutely along atomic lines and the only adjustable parameter is the electric-field value that is known only approximately from the voltage settings applied to the electrodes and slightly more precisely from the Stark spectrum itself. Considering the approximations made and the failure of the semiclassical approximation in the region of the maximum radius, near the caustic surface, the agreement between experiment and theory is very satisfactory. Some discrepancies are, of course, observed when comparing the relative intensities of the various fringes, however, their positions as well as most relative intensities are well reproduced by our calculations. Note that in this series of radial distributions, several of the images have been recorded on strong resonances, and others between resonances. The only difference (at least in this region of energy below E_{dir} where no competition between direct and indirect trajectories occur) that is experimentally noticeable in this case is the absolute intensity that is, of course, much larger on-resonance. At higher energy, and in particular above the direct threshold energy E_{dir}, images have been recorded but the experimental resolution is only partial due to the large density of fringes. As a consequence, the comparison is only qualitative and no direct comparisons are presented here.

The comparison between the experimental results and the semiclassical simulations is further illustrated in Fig. 13 where the positions of dark fringes in the experimental and the semiclassical images are shown as a function of the excitation energy above the saddle point, for a field strength of 615 V/cm. The comparison shows convincingly that the interferograms are well understood on the basis of the isotropic contribution calculated in the semiclassical model, at least in the limited region of energy where the experimental resolution is sufficient to observe the details of the interference pattern. The number of dark fringes observed is exclusively governed by the photoelectron excess kinetic energy and the strength of the electric field, and does not at all seem to depend on the approximate parabolic quantum numbers of the quasidiscrete Stark states excited, which cannot be properly defined in the case of a nonhydrogenic system such as xenon. The influence of being on- or off-resonance is mostly
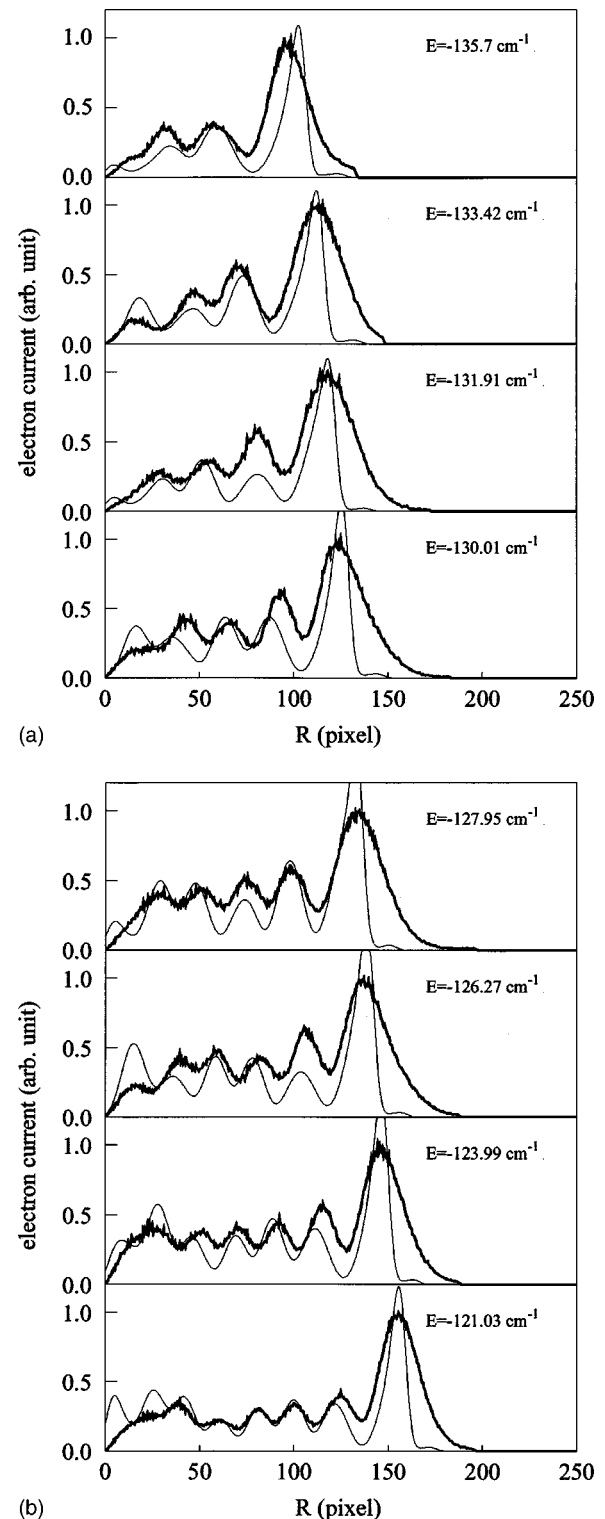

FIG. 12. Comparison between experimental measurements of the radial distribution $f(R)$ and semiclassical calculations. The electric field is $F=615$ V/cm. The energy ranges between 16.1 and 30.8 cm^{-1} above the saddle-point energy.

limited to the angular distribution as a function of angle θ and to the ratio of the direct and the indirect contribution in the image.

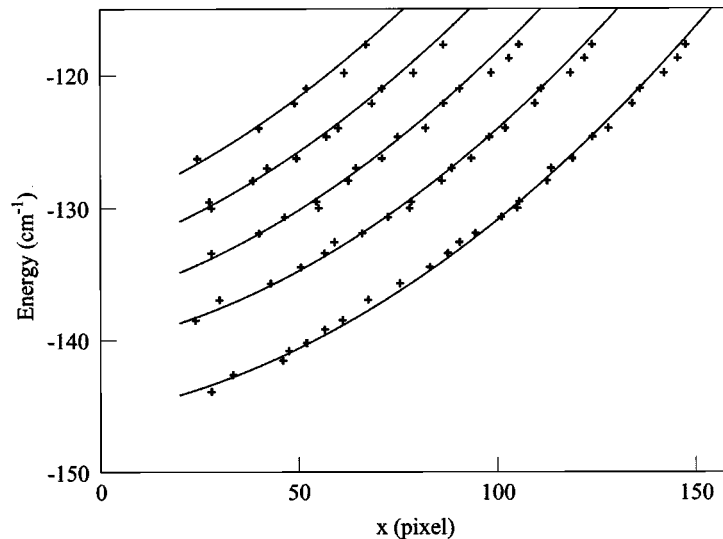We conclude that the extremely good agreement between

FIG. 13. Comparison of the experimental (+) and theoretical (thin solid line) position of dark fringes in the images, for images recorded in a dc electric field of 615 V/cm. The radius x is given in pixels. Only two varying parameters are used for this global comparison: the electric-field value (approximately determined from the electrode settings); and the magnification ratio (the proportionality factor between experimental and calculated radii) giving the absolute image size.

experiment and a theory based on an isotropic initial distribution of electron trajectories shows unambiguously that—contrary to predictions in the literature pertaining to atomic hydrogen [10]—interferograms for the photoionization of a nonhydrogenic atom such as xenon can be almost completely understood on the basis of continuum contributions and are not dominated by the nodal structures of well-defined quasi-discrete Stark resonances with given (n_1, n_2, m) parabolic quantum numbers. In other words, the system behaves as if the electrons were ejected isotropically with respect to the external electric field.

VI. CONCLUSION

The agreement between experiment and theory is remarkable given the assumptions made. In fact, most discrepancies between the experimental results and the semiclassical model are likely attributable to the semiclassical approximation itself. In addition to the failure of the semiclassical approximation when the electron momentum goes to zero, i.e., when the electron trajectory passes nearby the caustic surface, we have neglected the contribution of tunneling integrals. This is especially sensitive at the limit of the classically allowed region, i.e., on the external part of the image, but also at the peak of maximum intensity corresponding to the direct trajectories' component. The approximation can affect the relative intensity of the various interference fringes but gives the correct positions for the interferences. A full quantum calculation would undoubtedly lead to a better quantitative agree-

ment. These quantum calculations will be performed in the future in the framework of the generalized multichannel quantum-defect theory. Qualitatively, however, the overall features are already understood in the semiclassical approximation.

In conclusion, our results demonstrate without ambiguity that photoionization microscopy allows a deeper insight into ionization processes in an external electric field. Interference patterns corresponding to the transverse component of the Stark wave function have been observed. The continuum contribution is clearly dominant for a nonhydrogenic system such as xenon. Clearly, similar experiments on atomic hydrogen are required in order to clarify the distinction between parabolic states and continuum (or background contributions). Beyond a direct observation of the electronic wave function, photoionization microscopy provides a model system to access selected parts of the wave function and allows the construction of an atomic-size interferometer with potentially wide field of applications.

[1] R. R. Freeman, N. P. Economou, G. C. Bjorklund, and K. T. Lu, Phys. Rev. Lett. **41**, 1463 (1978).

[2] S. Feneuille, S. Liberman, J. Pinard, and A. Taleb, Phys. Rev. Lett. **42**, 1404 (1979).

[3] T. S. Luk, L. DiMauro, T. Bergeman, and H. Metcalf, Phys. Rev. Lett. **47**, 83 (1981).

[4] C. Blondel, C. Delsart, and F. Dulieu, Phys. Rev. Lett. **77**, 3755 (1996).

[5] C. Nicole, H. L. Offerhaus, M. J. J. Vrakking, F. Lépine, and Ch. Bordas, Phys. Rev. Lett. **88**, 133001 (2002).

[6] Yu. N. Demkov, V. D. Kondratovich, and V. N. Ostrovsky, Pis'ma Zh. Eksp. Teor. Fiz. **34**, 425 (1981) [JETP Lett. **34**, 425 (1981)].

[7] V. D. Kondratovich and V. N. Ostrovsky, J. Phys. B **17**, 1981 (1984).

[8] V. D. Kondratovich and V. N. Ostrovsky, J. Phys. B **17**, 2011 (1984).

[9] V. D. Kondratovich and V. N. Ostrovsky, J. Phys. B **23**, 21 (1990).

[10] V. D. Kondratovich and V. N. Ostrovsky, J. Phys. B **23**, 3785 (1990).

[11] J. Gao and J. B. Delos, Phys. Rev. A **49**, 869 (1994).

[12] Ch. Bordas, Phys. Rev. A **58**, 400 (1998).

[13] V. V. Beletzky, *Essays on the Motion of Celestial Bodies* (Mir, Moscow, 1977).

[14] H. A. Bethe and E. E. Salpeter, *Quantum Mechanics of One- and Two-Electron Atoms* (Springer, New York, 1957).

[15] L. D. Landau and E. M. Lifshitz, *Quantum Mechanics: Non-Relativistic Theory* (Addison-Wesley, Reading, MA, 1965).

[16] Some minor misprints in the formulas in Ref. [7] are corrected in the present paper.

[17] D. A. Harmin, Phys. Rev. A **24**, 2491 (1981).

[18] D. A. Harmin, Phys. Rev. Lett. **49**, 128 (1982).

[19] D. A. Harmin, Phys. Rev. A **26**, 2656 (1982).

[20] C. Nicole, I. Sluimer, F. Rosca-Pruna, M. Warntjes, M. J. J. Vrakking, C. Bordas, F. Texier, and F. Robicheaux, Phys. Rev. Lett. **85**, 4024 (2000).

[21] M. H. Rice and R. H. Good, J. Opt. Soc. Am. **52**, 239 (1962).

[22] *Handbook of Mathematical Functions*, edited by M. Abramowitz and I. A. Stegun (Dover, New York, 1965).

[23] A. T. J. B. Eppink and D. H. Parker, Rev. Sci. Instrum. **68**, 3477 (1997).

[24] H. L. Offerhaus, C. Nicole, F. Lépine, C. Bordas, F. Rosca-Pruna, and M. J. J. Vrakking, Rev. Sci. Instrum. **72**, 3245 (2001).